communications earth & environment

Article

https://doi.org/10.1038/s43247-024-01629-8

The orientation of intra-arc crustal fault systems influences the copper budget of magmatic-hydrothermal fluids

Daniele Tardani[1,2] ✉, Santiago Tassara[1] ✉, Pablo Sanchez-Alfaro[2,3], Martin Reich[2,4], Pamela Pérez-Flóres[5], Philippe Robidoux[2,4], Claudio Contreras[1,6], Daniele L. Pinti[7], José Cembrano[2,8] & Jay. J. Ague[9]

Some of the largest magmatic-hydrothermal copper ore deposits and deposit clusters are associated with arc-oblique fault systems. Whether this structural context impacts the geochemistry of hydrothermal fluids, including their copper contents, remains unknown. Here, we investigate the copper concentration and helium isotope signature of geothermal fluids as modern analogs of hydrothermal ore deposits in the Andes of central-southern Chile. We show that fault systems broadly parallel to the regional stress field facilitate the early release of fluids from deep primitive magmas. By contrast, fault systems oblique to the regional stress field prevent the early escape of fluids and promote magmatic enrichment in copper, volatiles, and ligands, enhancing the potential to form copper deposits. We conclude that the orientation of fault systems actively influences the copper budget of ascending hydrothermal fluids, explaining the contrasting distribution of metals along distinct structures often observed in porphyry-epithermal systems and other types of magmatic-hydrothermal deposits.

Copper's criticality stems from its broad range of industrial applications, particularly its key role in advancing green energy technologies and electrification infrastructure. The Earth's crust typically contains copper (Cu) concentrations of less than 30 ppm[1], making its economic extraction viable only in ore deposits. Magmatic-hydrothermal deposits such as porphyry Cu-Mo-Au and related epithermal Au-Ag systems are a primary source of global copper and gold production and supply considerable amounts of molybdenum and silver, among other critical elements, including rhenium[2,3]. Most commonly found in subduction zones, porphyry-epithermal systems are formed by the efficient transport and accumulation of ore metals that precipitate predominantly as sulfides from hydrothermal fluids released from evolving arc magmas[4–6]. Although it is increasingly recognized that oxidizing conditions and elevated concentrations of water, sulfur, and halogens in arc magmas are essential to the formation of porphyry-epithermal deposits over Earth's history[7–9], the mechanisms governing the occurrence of both fertile and barren magmatic-hydrothermal systems within restricted arc segments remain puzzling[10].

An increasingly recognized hypothesis holds that the ore metal fertility of a productive crustal domain is given by a combination of processes operating during the evolution of magmas and fluids throughout the whole lithospheric column[6,11–13]. These include the production of oxidized magmas rich in water and ligands[10,14–16], metal enrichment in the magma sources or their melting products[17–19], the efficiency of metal and ligand transfers from magmas to hydrothermal fluids[20,21], the duration of the magmatic-hydrothermal activity in the shallow crust[22], and the efficiency of ore precipitation[13]. Another important factor relates to the intricate nature of transcrustal/deep-seated structural controls on magma emplacement and fluid circulation, which can significantly influence ore formation[23,24]. A recent view argues that the most favorable structural conditions for the formation of an intrusion-related hydrothermal ore system are provided by deep-seated

[1]Instituto de Ciencias de la Ingeniería, Universidad de O'Higgins, Rancagua, Chile. [2]Andean Geothermal Center of Excelence (CEGA), Facultad de Ciencias Físicas y Matemáticas, Universidad de Chile, Santiago, Chile. [3]Instituto de Ciencias de la Tierra, Facultad de Ciencias, Universidad Austral de Chile, Valdivia, Chile. [4]Departamento de Geología, Facultad de Ciencias Físicas y Matemáticas, Universidad de Chile, Santiago, Chile. [5]Consultoría e Investigación Geológico Ambiental Ltda. (CIGEA Ltda.), Huasco, Chile. [6]School of Earth Sciences, University of Bristol, Bristol, UK. [7]GEOTOP and Département des Sciences de la Terre et de l'Atmosphère, Université du Québec à Montréal, Montréal, QC, Canada. [8]Departamento de Ingeniería Estructural y Geotécnica, Pontificia Universidad Católica de Chile, Santiago, Chile. [9]Department of Earth and Planetary Sciences, Yale University, New Haven, CT, USA. ✉e-mail: daniele.tardani@uoh.cl; santiago.tassara@uoh.cl

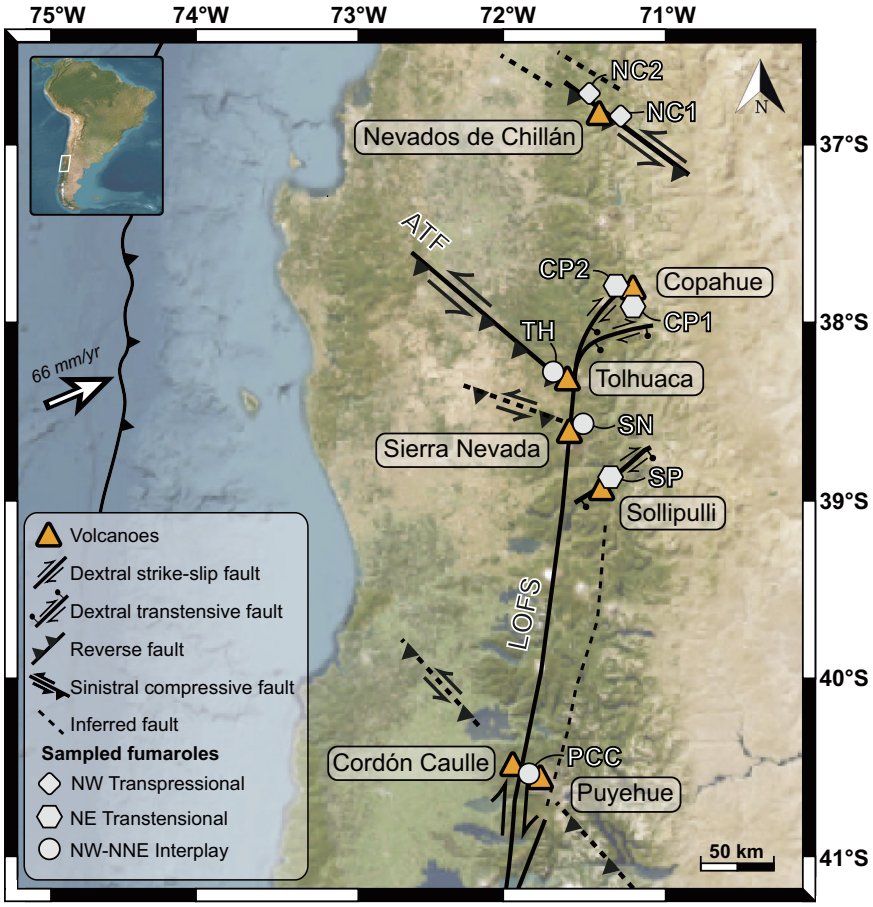

Fig. 1 | Simplified structural map of the central portion of the Southern Volcanic Zone (SVZ) of Chile. Solid and dashed lines represent mapped and inferred faults, respectively. Circles, hexagons, and diamonds indicate the location of fumarole samples associated with different structural domains. A detailed version of this map is presented in Supplementary Fig. S1. ATF Andean Transverse Faults, LOFS Liquiñe-Ofqui Fault Systems, NC Nevados de Chillan, PCC Puyehue-Cordón Caulle, SN Sierra Nevada, TH Tolhuaca, SP Sollipulli, CP Copahue.

faults oriented at a high angle with respect to the maximum principal the regional stress, i.e., fault systems that are misoriented for reactivation with respect to the prevailing stress field[25,26]. Such misoriented faults may promote magmatic differentiation at depth, leading to increasing residence times and multi-episodic magmatic recharge processes that ramp up the volatile content of magmas[7,13,27]. Accumulation of magma-derived volatiles favors host rock hydraulic fracturing at nearly lithostatic fluid pressures fostering positive feedback between fracturing and fluid flow[28]. Also, the elevated water and ligand content of magmas is expected to result in a more efficient transfer of ore metals such as Cu to hydrothermal fluids[8,29,30]. Although crustal thickening is considered a first-order control on metal transport and concentration in ore systems[10,31,32], the structural controls on magmatic-hydrothermal plumbing systems and ore metal enrichment—and thus, their impact on the size and grade of the deposit—remain essentially unknown. This challenge is mainly because ore deposits represent fossil magmatic-hydrothermal systems that record a time-integrated sequence of fluid-flow pulses, hindering direct estimations of the enhancing effect that fault systems may have on mineralization events.

We tackle this gap in knowledge by determining the variations in the Cu concentration of fluids sampled from active hydrothermal systems in central-southern Chile as modern analogs of shallow mineralizing systems[33–35]. We do this by sampling subaerial fumaroles and associated hot springs that occur in contrasting volcano-tectonic domains. A key advantage of our case scenario is that the interaction between magmatism, hydrothermal activity, and seismicity in contrasting volcano-tectonic domains is well established[27,34,36–39]. By combining the chemical and helium isotopic composition of fumarole gases and related hot spring waters sampled along different structural domains, we show that the nature of fault systems actively influences the Cu budget of ascending hydrothermal fluids.

Results and discussion

Volcano-tectonic domains

The studied fumaroles and hot springs are associated with active Pleistocene-to-Holocene stratovolcanoes and are distributed along a ~450 km segment (36°–40°S) of the central and southern portions of the Chilean Southern Volcanic Zone (SVZ) (Fig. 1). The thickness of the continental crust in this segment (approximately ~40 km) varies little along-strike and is located above a slightly shallow dipping (<25°) Benioff zone[40].

Figure 1 shows the location of the studied hydrothermal manifestations and a simplified sketch of the main associated structural features. A detailed structural map is reported in Supplementary Material Fig. S1. Geophysical data, including magnetotelluric, ambient seismic noise Rayleigh-wave tomography, and InSAR inversion data suggest that these structural features exert a first-order control on the magmatic-hydrothermal plumbing system (Supplemental Material Table S1). As such, the volcanic and hydrothermal activity of this segment can be classified into three main volcano-tectonic domains, as follows.

1. A transtensional domain is associated with an NE striking network of extensional and extensional shear fractures that are broadly parallel to the current maximum horizontal stress in the SVZ (*hereafter* NE transtensional) (Fig. 1; Supplementary Material Fig. S1; Methods). These faults-fracture networks typically form under relatively low differential stress and correspond to secondary structures of the intra-arc NNE-striking dextral strike-slip Liquiñe Ofqui Fault Systems or to transverse ENE-striking basement faults[36,41]. NE faults can, for instance, form pull-apart structures in accommodation zones or act as transtentional faults under volcanic systems[42]. Under the NE-transtensional domain, the magmatic plumbing system is dominated by interconnected vertical faults and tension cracks favoring a rapid ascent of basaltic to basaltic-andesite magmas from the deep crust with little crustal inputs[27,43].

Table 1 | Location, chemical, and rare gases isotope data of sampled hot spring and fumarole samples from the Southern Volcanic Zone of Chile

Sample	Volcanic center	Location UTM (19 H)		Altitude	T (°C)	pH[a]	TDS[a]	S_L[a]	Cl[a]	Cu[a]	Co[a]	Ni[a]	CO_2[b]	S_{tot}[b]	R/Ra	±	Rc/Ra	±	He/Ne
		E	S	(m.a.s.l.)			mg/L	mg/L	mg/L	µg/L	µg/L	µg/L	%	%					
NC1	Nevado de Chillan	286143	5912904	2032	83	2.6	440	96.9	16.62	6.3	5	7	77.5	15.5	3.40	0.07	3.54	0.02	5.74
NC2	Nevado de Chillan	286122	5912741	1975	91	2.4	1486	291	11.82	25.4	13.8	26	72.99	12.86	3.40	0.07	3.68	0.10	3.05
CP1	Copahue	316314	5812167	2021	94	2.8	799	136.8	0.32	0.92	0.25	0.6	92.20	1.2	7.57	0.15	7.59	0.01	27.17
CP2	Copahue	316586	5810563	1992	93	2.1	1490	440.9	2.5	1.81	0.47	2.41	94.10	0.73	7.48	0.15	7.52	0.01	471.5
TH	Tolhuaca	268800	5756321	2609	92	2.4	874	212.9	5	4.78	8.37	5.11	95.22	1.1	6.38	0.13	6.49	0.05	16.07
SN	Sierra Nevada	272121	5727163	1508	88	3	321	57.4	2.2	3.5	1.1	1.43	86.42	4.74	4.59	0.09	4.61	0.01	51.34
SP	Sollipulli	274931	5681429	1396	95	2.6	600	49.5	1.37	0.29	0.052	0.92	93.85	0.65	5.88	0.05	7.72	0.42	1.16
PCC	Puyehue-Cordón Caulle	740614	5513347	1546	95	2.4	2156	480.2	13.6	24.17	12.7	9.43	93.2	4.73	5.42	0.2	5.74	0.22	4.85

m.a.s.l. is meters above sea level.
[a]Measured in the acidic hot spring waters (*TDS* total dissolved solids; S_L is total sulfur measured as SO_4^{2-} in the acidic waters).
[b]Measured in the fumarole gas samples.

2. A compressional to the transpressional domain is associated with a network of NW-striking faults and subhorizontal cracks (*hereafter* NW transpressional) (Fig. 1; Supplementary material Fig. S1; Methods). In this domain, the controlling NW faults are oriented at a high angle with respect to the current maximum horizontal stress in the SVZ (σ_1 = N60E) and can only be activated by fault-valve mechanisms that require supra-lithostatic fluid pressures[25,36]. Plumbing systems associated with this compressional regime favor relatively shallow (<10 km) magma reservoirs, longer residence times, and episodic magma fractionation forming basaltic to rhyolitic volcanic products[27] (Supplementary Material Table S1).
3. A third volcano-tectonic association occurs where the NW striking faults intersect with the transcurrent NNE striking faults of the intra-arc Liquiñe-Ofqui Fault Systems (*hereafter* NW-NNE interplay), forming a local combined compressional and strike-slip regime (Fig. 1; Supplementary Material Fig. S1; Methods). In this case, both systems are likely to accommodate deformation depending on local and transient changes in the stress field[36,37]. In this structural regime, the magmatic plumbing system is tapped by NW compressive faults and fed by deep crustal inputs that ascend through the deep-seated transcurrent NNE faults[27].

Sampled hydrothermal fluids

A total of eight shallow fumarole gas and hot spring water samples were used in this study, spanning the three main tectonic-magmatic domains mentioned above. Sampling sites represent all currently known stratovolcano-related hydrothermal systems with active fumaroles within the 36°–40°S segment of the SVZ. Two samples are associated with a purely NW transpressional domain (NC1, NC2, Nevados de Chillán; Fig. 1), three samples are associated with purely NE transtensional domains (CP1, CP2, Copahue; SP, Sollipulli; Fig. 1), and three samples were collected in systems related with the NW-NNE interplay domain (TH, Tolhuaca; SN, Sierra Nevada; PCC, Puyehue-Cordón Caulle; Fig. 1).

To obtain representative values for sulfur, carbon dioxide content, helium isotope ratios, and trace metal concentration of the hydrothermal fluids, we sampled both the acidic hot spring waters and the associated fumarole gas at the surface. The acidic waters are produced by the natural condensation of water vapor in the fumarole gas due to the temperature drop close to the surface, capturing the acid species (SO_2, HCl, HF) and metals[44]. The fumarole gases were also condensed through a cooling system to preserve the metal content remaining in the gas phase after the natural condensation process (See Methods). All samples were collected in sites where it was possible to obtain both the gas (for the analysis of S_{tot}, CO_2, and $^3He/^4He$ ratios) and the highly acidic waters (pH < 3; for Cu, Co, and Ni analyses), this strategy allowed to obtain representative data of the magmatic-hydrothermal system. Sulfur was measured both in the gas (as $S_{tot} = SO_2 + H_2S$) and in the acidic waters (S_L = S in SO_4^{2-}).

Sources and composition of the hydrothermal fluids

The chemical and isotopic composition of gases and water are reported in Table 1. The concentration of CO_2 and S_{tot} in gases ranges from 72.99% to 95.22% and 0.65% to 15.5%, respectively. The SO_2 species, along with HCl and HF, are mostly scrubbed (dissociated in water) when the water vapor condenses during ascent towards the surface[45].

Helium isotopes ($^3He/^4He$) are expressed as Rc/Ra, which is the air-corrected $^3He/^4He$ ratio of the sample (Rc; See Methods) over the present-day $^3He/^4He$ atmospheric ratio ($Ra = 1.384 \times 10^{-6}$)[46]. Because ^4He is derived from the radiogenic decay of U-Th, the Earth's crust is mainly dominated by ^4He with low Rc/Ra ratios (0.05)[47] while the depleted mantle shows elevated Rc/Ra ratios (8 ± 1)[48], caused by the presence of the preserved primordial ^3He isotope. These contrasted ratios between the atmosphere, the crust, and the mantle reservoirs are very useful to distinguish the sources of volatiles in a hydrothermal system[49]. The Rc/Ra of sampled fumaroles range between 3.54 and 7.80, with an analytical error <0.5 (Table 1; Methods). All the fumarole gas samples display much

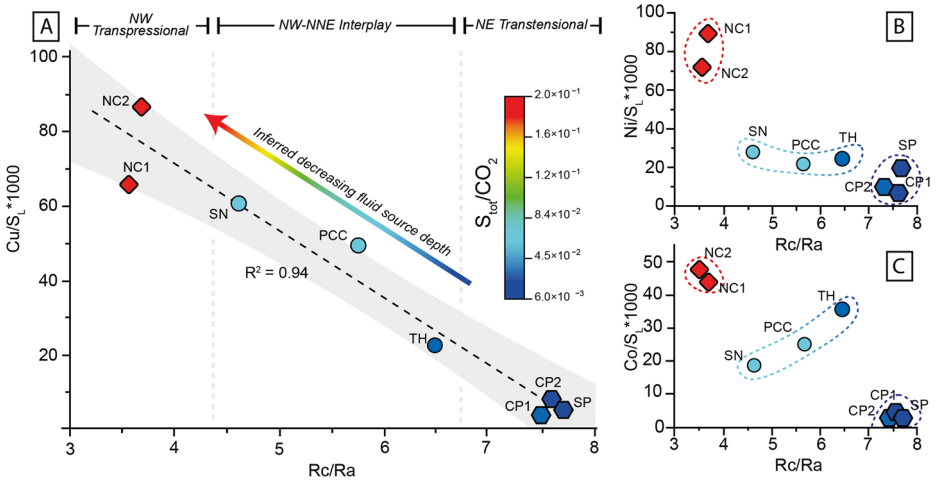

Fig. 2 | Binary plots showing the helium isotope and metal composition of modern hydrothermal fluids in the SVZ. A Cu/S_L*1000 vs. Rc/Ra. Linear trendline ($R^2 = 0.94$) and 95% confidence interval is reported. The color gradient bar represents the S_{tot}/CO_2 ratio of each sample. **B**, **C** show the Rc/Ra vs. Ni/S_L*1000 and Co/S_L*1000, respectively. Error margins are lower than each mark size (see Methods). NC Nevados de Chillan, PCC Puyehue-Cordón Caulle, SN Sierra Nevada, TH Tolhuaca, SP Sollipulli, CP Copahue.

higher Rc/Ra ratios than purely crustal values, indicating that the whole studied crustal segment receives a strong contribution of mantle-derived helium. However, whereas samples associated with the NW transpressional domain (NC1, NC2) present the most radiogenic Rc/Ra values (3.54 and 3.68, respectively), samples associated with NW-NNE interplay (TH, SN, PCC) present moderately radiogenic values (4.61 and 5.70), and samples in the NE transtensional domain (CP1, CP2, SP) exhibit mantle Rc/Ra values between 7.52 and 7.72. The similarity between the Rc/Ra of hydrothermal fluids and fluid inclusions in associated volcanic rocks further supports a magmatic primary source of volatiles in the sampled fumaroles with limited to no modifications after fluid exsolution[50–52]. In addition, the correspondence of Rc/Ra ratios in hydrothermal fluids with literature Sr isotope data in the associated volcanic rocks suggest that Rc/Ra variations are related to radiogenic crustal inputs to the magmatic reservoir during differentiation prior to fluid exsolution[37,50].

Copper was detected in all the acidic water samples. Its content, along with the S_L, Cl, and other base metal concentrations, are presented in Table 1. Most of the metal concentrations in the gas condensates are negligible, indicating that the metal load of the ascending hydrothermal fluids partitions into the liquid phase. The narrow range of water pH, between 2.2 and 3, and the overall similar nature of the sampled systems exclude the possible change in Cu and S solubility in water due to shallow processes, ensuring that the metal concentrations reflect only variations in the fluid's source[44]. Low-temperature hydrothermal fluids are the ultimate result of a complex evolution of more primary, high-temperature, magmatic-hydrothermal fluids that may have undergone cooling and expansion, brine condensation and/or precipitation of metal-bearing phases, and/or scrubbing processes[53]. Nonetheless, all sampled systems occur within a similar geodynamic setting, and fluids share physicochemical features (e.g., temperature and pH) that suggest analogous evolutionary pathways. The Cu composition of the hydrothermal fluids is expressed as Cu/S_L ratios (and not absolute Cu concentrations) to avoid the metal content variability that may be due to the unquantifiable degree of mixing with surficial waters, this provides a more reliable measure of their primary metal composition and allows comparisons of samples from different systems. Notably, the Cu/S_L ratios of our samples are comparable to those reported for high-temperature volcanic gases and ore-forming fluids[53–55]. In addition, the distinctive correlation of Cu/S_L with independent geochemical proxies—such as Rc/Ra and S_{tot}/CO_2—strongly suggests that the Cu/S_L ratio responds to primary fluid compositional variations (Fig. 2, see below). Therefore, and although the absolute Cu concentration of the acidic waters is lower than those typically found in high-temperature volcanic gasses and fluid inclusions[53,55], we posit that the Cu/S_L ratio of the sampled hot springs stands as a reliable proxy to compare Cu compositional variabilities in magmatic-hydrothermal fluids.

Figure 2A shows that the Cu/S_L ratio negatively correlates with the Rc/Ra ratio ($R^2 = 0.95$). The color gradient in Fig. 2A illustrates the correspondence of the Cu/S_L vs. Rc/Ra correlation with the S_{tot}/CO_2 ratio of the hydrothermal fluids. The S_{tot}/CO_2 ratio serves as a proxy of the fluid exsolution depth. Under higher pressure conditions, less soluble gas species in magmas like CO_2 are exsolved (even at depths of over 25 km), whereas more soluble species such as H_2S and SO_2 are released at later stages at shallower depths[56,57]. Thus, increasing S_{tot}/CO_2 ratios reflect the decreasing depth of fluid exsolution. Nonetheless, we warrant caution in this interpretation, given the low-temperature and shallow nature of the studied systems. Figure 2A shows that samples containing deep magmatic volatiles —corresponding to higher Rc/Ra—have lower Cu/S_L and were likely sourced at greater depths. By contrast, samples with more radiogenic He contributions (lower Rc/Ra) have higher Cu/S_L and were most likely produced at shallower crustal depths. In addition, Ni/S_L and Co/S_L also show a negative correspondence with Rc/Ra (Fig. 2B, C and Table 1). Copper, Ni, and Co have similar geochemical behavior and partitioning into similar phases during the magma differentiation, including in mantle and crustal magmatic sulfides as well as in hydrothermal sulfides in both active and fossil systems[18,20,35,58,59]. The Ni/Cu and Co/Cu ratios of our samples (Table 1) are consistent with the same ratios in magmatic sulfides and volcanic fumaroles in arc settings (e.g., Merapi volcano, Indonesia), pointing to a potential source relationship[20]. However, unlike Cu, Co, and Ni also present a lithophile affinity during magmatic differentiation, which may explain some of the dispersion in Fig. 2B, C.

Structural controls on the Cu concentration of hydrothermal fluids

Tectonic and magmatic processes in the porphyry-epithermal environment result in the formation of high permeability conduits that efficiently focus and transport ore-forming fluids[28]. An increasing body of evidence suggests that giant porphyry Cu deposits (e.g., El Salvador, Spence, Centinela, and Escondida) and deposit clusters tend to form in association with compressional to transpressional faults that are oblique with respect to the regional stress field[25,26]. This structural configuration is thought to limit the ascent of magmas, which in turn promotes further differentiation and fluid accumulation, increasing the ore-forming potential of a magmatic-hydrothermal system[25]. We argue that this optimal structural configuration also impacts the Cu budget of fluids based on the contrasting Cu/S_L vs. Rc/Ra signature of modern hydrothermal fluids associated with different structural arrays.

Our data reveal three main cases that relate the helium isotopes and metal composition of hydrothermal fluids to the structural domains recognized in the Chilean SVZ. On the one hand, samples associated with NE transtensional structural domains display the highest (most primitive)

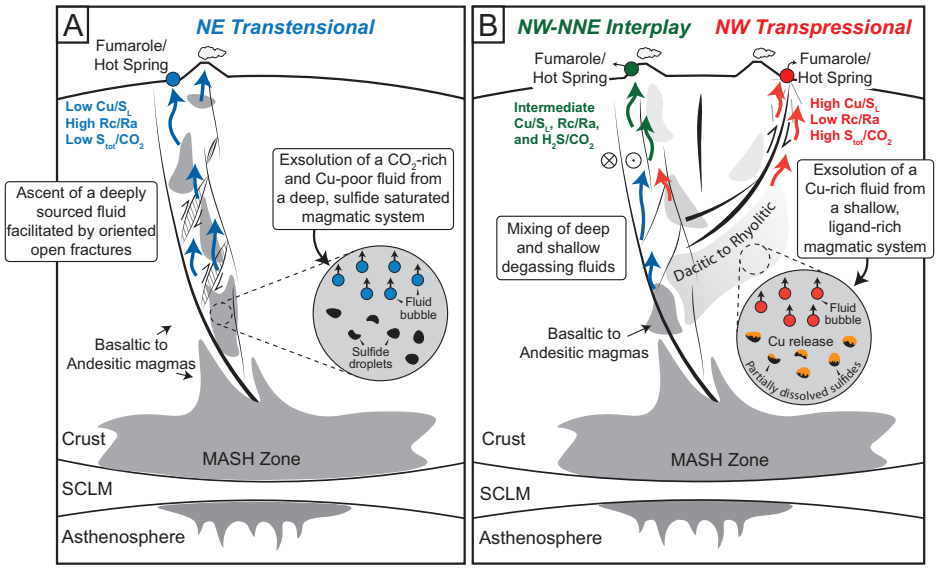

Fig. 3 | Conceptual model of the structural-geochemical links in variable volcano-tectonic domains. A Optimally oriented NE transtensional faults promote fluid to escape from deep and primitive magmatic systems where Cu remains mainly in the magma at the time of fluid exsolution (in silicate melt or sulfides). Panel **B** shows both the hydrothermal systems associated with the NW transpressional faults (red), where hydrothermal fluids form from a more evolved, ligand-rich magma, scavenging Cu more efficiently (form silicate melt or sulfides). Systems associated with the NW-NNE interplay (green) are also represented in panel **B**, where the mixture with deeply sourced fluids leads to intermediate compositions.

Rc/Ra signatures, the lowest Cu/S_L ratios, and the lowest S_{tot}/CO_2 ratios (Fig. 2). On the other hand, samples associated with the NW transpressional structural domain show the lowest Rc/Ra ratios and the highest Cu/S_L and S_{tot}/CO_2 ratios (Fig. 2). Finally, samples associated with the NW-NNE interplay domain have intermediate Rc/Ra, Cu/S_L, and S_{tot}/CO_2 ratios (Fig. 2).

A conceptual model that explains the three observed scenarios is presented in Fig. 3. The crustal faults of the NE transtensional domain (Fig. 3A), optimally oriented for opening with respect to the regional stress field, promote the deep exsolution of hydrothermal fluids facilitated by the formation of open fractures[36]. Thus, fluid exsolution is produced from a deep and relatively primitive source, consistent with the high measured Rc/Ra and low S_{tot}/CO_2 values. These NE transtensional faults networks prevent fluid accumulation and magmatic differentiation and, thus, source magmas may have not yet evolved to a stage where the concentration of ligands such as Cl is high enough to allow efficient extraction of Cu and other metals from magma[8,10]. This is consistent with the more mafic character of erupted products in these volcanic systems[27]. The favorable scenario for Cu ore formation is shown in Fig. 3B, where the dominant structural control is exerted by faults of the NW transpressional domain. Because these structures are misoriented for reactivation with respect to the regional stress field, they prevent the early separation of fluids from magmas. Instead, they promote increasing residence times and magmatic differentiation and produce magmatic enrichment in volatiles and ligands, leading to a more efficient Cu extraction at the time of fluid exsolution[29]. Their lower Rc/Ra values are explained by either interaction with crustal materials or by the magmatic production of radiogenic He (magma aging) associated with their more protracted residence times[50]. Fluids separated at this stage would thus present relatively high contents of Cu and can migrate through the shallow local faults controlling the hydrothermal system. The sourced Cu may be in the silicate melt fraction or in the sulfide phases of a saturated magma that could be redissolved to transfer their metal load to the hydrothermal fluid[20,60]. The latter is consistent with the similarity of the Ni/Cu and Co/Cu ratios of hydrothermal fluids and magmatic sulfides reported in volcanic systems in arcs[20]. As such, in the NW transpressional domain, fluids are characterized by radiogenic He isotope compositions, higher S_{tot}/CO_2 ratios, and higher Cu/S_L. Finally, in the NW-NNE interplay domain (Fig. 3B), the misoriented fault systems promote magmatic differentiation and fluid accumulation as in the previous scenario. However, the interplay with the deep-seated NNE-striking transcurrent faults also allows the involvement of deep magmatic or hydrothermal inputs from more primitive sources. As a result, the hydrothermal fluids represent the mixing of two contrasting endmembers.

It is relevant to note that the relative paucity of economic ore deposits in the studied area is likely the result of fundamental tectono-magmatic conditions, such as the effects of the crustal thickness on the low initial Cl and S composition of near-primary melts[10]. The hydrothermal systems studied here occur within a mostly barren crustal segment of relatively homogeneous thickness. Thus, the variable structural configurations allow us to better examine the extent to which fault systems that control the ascent of magmas can impact the geochemistry of fluids. Whereas active fault systems misoriented for reactivation are favorable for ore formation (fluids with higher Cu/S_L and lower Rc/Ra), the presence of fault systems optimally oriented for reactivation is unfavorable for the genesis of coeval magmatic-hydrothermal ore deposits (fluids with lower Cu/S_L and higher Rc/Ra). These results align well with helium isotope data extracted from fluid inclusions within various mineralized systems worldwide, including porphyry Cu, epithermal Au-Ag, and skarn deposits (see Supplementary Material Table S2). Such deposits are formed by hydrothermal fluids derived from variably evolved arc magmas with low Rc/Ra ratios, between ~3 and ~0.2 (Supplementary Material Table S2). Our study reveals variable Rc/Ra ratios in geothermal manifestations of the SVZ, with the lowest values (Rc/Ra ~3.5) in the Cu-richest samples NC1 and NC2. The lowest Rc/Ra values that we observe draw near the fertile systems' threshold, in agreement with their association with the NW transpressional domain, their higher Cu/S_L ratio, and the role of misoriented fault systems on the fertility of hydrothermal systems. Our results highlight that the structures associated with magmatic-hydrothermal systems can contribute to modulating the Cu budget of produced fluids, ultimately impacting the location and size of a magmatic-hydrothermal deposit. Similar examples may include Andean-type iron oxide-copper-gold (IOCG) and iron oxide-apatite (IOA) systems, which occur within the world-class metallogenic province of the Coastal Cordillera in central-northern Chile and southern Perú[61–63]. The formation of IOA and IOCG deposits was intimately associated with the activity of the sinistral strike-slip Atacama Fault System during the early Cretaceous[64]. As reported[27,65], Fe-(±Ti-V)-rich and Cu-S-poor IOA deposits occur mostly along the NNE principal trace of the fault, while Cu-S-rich IOCG systems often occur along NW structures, pointing to structurally driven Fe vs. Cu partitioning. Finally, this study also supports the hypothesis that essential tectono-magmatic elements, such as increasing crustal thickness and elevated volatile contents, need to be given for an arc segment to be productive. Our conclusions contribute to understanding the local variations that produce barren and Cu-rich deposits within restricted arc segments of the same age and crustal thickness, having direct implications for conceptual mineral exploration.

Methods

Sampling and analysis of fumarole gases, fumarolic condensates, and acidic waters

Fumarole gases were sampled using a titanium tube, inserted into the fumarole vent, and connected to a condenser to force the separation of a dry gas and a fumarolic condensate. The dry gas aliquot for chemical components and helium isotope analysis was collected in pre-evacuated alkaline glass containers with vacuum valves at both ends. This method for volcanic gas sampling is exhaustively described by ref. 37. Both fumarolic condensates and hot spring water samples were collected in pre-cleaned high-density polyethylene bottles and were analyzed for their chemical composition.

Six out of eight helium, CO_2, and S_{tot} data have been documented in prior works[37,66]. The chemical composition (S_{tot} and CO_2) of sampled gases was measured using a quadrupole mass spectrometer. Experimental errors are ±10%. The gas mixture in the copper tubes was diluted manually in a constant volume until reaching a pressure lower than 10 mbar. The reactive gases (e.g., H_2O) were removed using two Ti-getter, operated at 600 °C for 15 min, followed by 10 min at ambient temperature. One SAES ST-707 getters were also used at 100 °C for 15 min followed by 10 min at ambient temperature. Gases were then adsorbed onto an Advanced Research System cryogenic trap containing activated charcoal at 10 K and released at 40 K for He and 90 K for Ne. He and Ne isotopes were measured at the Montreal Noble Gas Laboratory (GRAM) of GEOTOP on a Thermo® HELIX-MC Plus using an axial Faraday detector by peak, except for ^{3}He, which was measured by ion counting on an axial Compact Discrete DynodeTM (CDD) detector. Obtained signals were calibrated against standard air. Blanks are typically on the order of 0.01% for He and Ne. Typical standard reproducibility for ^{4}He and ^{20}Ne are 1.5–2%. Errors on the ^{3}He/^{4}He ratios are 2% at 1σ for high ^{3}He (magmatic) samples.

The measured ^{3}He/^{4}He ratios, normalized to the atmosphere $Ra = 1.384 \times 10^{-6}$, have been corrected for the presence of atmospheric helium (Rc/Ra) using the ^{4}He/^{20}Ne ratio of the sample[67]:

$$\frac{R_c}{R_a} = \left(\frac{R}{R_a} - r\right)/(1 - r) \quad (1)$$

where "r" is:

$$r = \left(\frac{^4He}{^{20}Ne}\right)_{ATM} \Big/ \left(\frac{^4He}{^{20}Ne}\right)_{obs} \quad (2)$$

where $(^4He/^{20}Ne)_{ATM}$ and $(^4He/^{20}Ne)_{obs}$ are the atmospheric and observed ^{4}He/^{20}Ne ratios, respectively.

Anions (Cl, S) of hot spring waters were analyzed in ACTLABS laboratories in Canada using an Ion Chromatography (IC, Dionex ICS 2100) with the reported errors of Cl = ± 0.15 mg/L and S = ± 0.1 mg/L, and detection limits of Cl = 0.3 mg/L and S = 0.3 mg/L. Concentrations of trace elements (Cu, Co, Ni) were analyzed in ACTLABS using an Inductively Coupled Plasma–Mass Spectrometry (ICP-MS; iCap). Reported errors are the following, Cu = ±0.2 µg/L, Co = ±0.03 µg/L; Ni = ±0.4 µg/L. Detection limits are the following, Cu = 2 µg/L, Co = 0.05 µg/L; Ni = 3 µg/L.

Structural map

The regional and local structural domains documented in this work were defined using a combination of photointerpretation on Digital Elevation Models and quick bird images (from Google Earth), and a compilation of previous works described in Supplementary Fig. S1.

Online content

Any methods, additional references, Nature Research reporting summaries, source data, statements of code and data availability, and associated accession codes are available in the supplementary information.

Data availability

The data generated or analyzed during this study are included in this published article and its Supplementary Information and Supplementary Data files.

Received: 22 January 2024; Accepted: 14 August 2024;
Published online: 02 September 2024

References

1. Rudnick, R. L. & Gao, S. in *Treatise on Geochemistry*. (eds. Holland, H. D. & Turekian, K. K.) Vol. 3, The Crust 1–64 (Elsevier-Pergamon, Oxford, 2003).
2. Cooke, D. R., Hollings, P., & Walsh, J. L. Giant porphyry deposits: Characteristics, distribution, and tectonic controls. *Econ. Geol*. **100**, 801–818 (2005).
3. John, D. A. & Taylor, R. D. By-products of porphyry copper and molybdenum deposits. *Rev. Econ. Geol*. **18**, 137–164 (2016).
4. Hedenquist, J. W. & Lowenstern, J. B. The role of magmas in the formation of hydrothermal ore deposits. *Nature* **370**, 519–527 (1994).
5. Heinrich, C. A. & Candela P. A. in *Treatise of Geochemistry* (second edition). 1–28 (Elsevier, 2014).
6. Park, J.-W., Campbell, I. H., Chiaradia, M., Hao, H. & Lee, C.-T. Crustal magmatic controls on the formation of porphyry copper deposits. *Nat. Rev. Earth Environ.* **2**, 542–557 (2021).
7. Audétat, A. & Simon, A. C. Magmatic controls on porphyry copper genesis. In *Geology and Genesis of Major Copper Deposits and Districts of the World: A Tribute to Richard H. Sillitoe: Society of Economic Geologists Special Publication*, Vol. 16 (eds. Hedenquist, J.W., Harris, M. & Camus, F.), 553–572 (2012).
8. Tattich, B., Chelle-Michou, C., Blundy, J. & Loucks, R. R. Chemical feedbacks during magma degassing control chlorine partitioning and metal extraction in volcanic arcs. *Nat. Commun.* **12**, 1774 (2021).
9. Meng, X. et al. Oxidized sulfur-rich arc magmas formed porphyry Cu deposits by 1.88 Ga. *Nat. Commun.* **12**, 2189 (2021).
10. Grondahl, C. & Zajacz, Z. Sulfur and chlorine budgets control the ore fertility of arc magmas. *Nat. Commun.* **13**, 4218 (2022).
11. Richards, J. Giant ore deposits formed by optimal alignments and combinations of geological processes. *Nat. Geosci.* **6**, 911–916 (2013).
12. Muntean, J. L., Cline, J. S., Simon, A. C. & Longo, A. A. Magmatic–hydrothermal origin of Nevada's Carlin-type gold deposits. *Nat. Geosci.* **4**, 122–127 (2011).
13. Wilkinson, J. J. Triggers for the formation of porphyry ore deposits in magmatic arcs. *Nat. Geosci.* **6**, 917–925 (2013).
14. Lee, C.-T. A. & Tang, M. How to make porphyry copper deposits. *Earth Planet. Sci. Lett.* **529**, 115868 (2020).
15. Rezeau, H. & Jagoutz, O. The importance of H_2O in arc magmas for the formation of porphyry Cu deposits. *Ore Geol. Rev.* **126**, 103744 (2020).
16. Ague, J. J. et al. Slab-derived devolatilization fluids oxidized by subducted metasedimentary rocks. *Nat. Geosci.* **15**, 320–326 (2022).
17. Chiaradia, M. Distinct magma evolution processes control the formation of porphyry Cu–Au deposits in thin and thick arcs. *Earth Planet. Sci. Lett.* **599**, 117864 (2022).
18. Tassara, S. et al. Plume-subduction interaction forms large auriferous provinces. *Nat. Commun.* **8**, 843 (2017).
19. Tassara, S. et al. Osmium isotopes fingerprint mantle controls on the genesis of an epithermal gold province. *Geology* **50**, 1291–1295 (2022).
20. Nadeau, O., Williams-Jones, A. & Stix, J. Sulphide magma as a source of metals in arc-related magmatic hydrothermal ore fluids. *Nat. Geosci.* **3**, 501–505 (2010).
21. Blundy, J. et al. Generation of porphyry copper deposits by gas–brine reaction in volcanic arcs. *Nat. Geosci.* **8**, 235–240 (2015).

22. Chelle-Michou, C. et al. Tempo of magma degassing and the genesis of porphyry copper deposits. *Sci. Rep.* **7**, 40566 (2017).
23. Weimer, D. et al. Ancient structural inheritance explains gold deposit clustering in northern Perú. *Geology* **50**, 1197–1201 (2022).
24. Jørgensen, T. R. C. et al. The implications of crustal architecture and transcrustal upflow zones on the metal endowment of a world-class mineral district. *Sci. Rep.* **12**, 14710 (2022).
25. Piquer, J., Sanchez-Alfaro, P. & Pérez-Flores, P. A new model for the optimal structural context for giant porphyry copper deposit formation. *Geology* **49**, 597–601 (2021).
26. Farrar, A. D. et al. A model for the lithospheric architecture of the central andes and the localization of giant porphyry copper deposit clusters. *Econ. Geol.* **118**, 1235–1259 (2023).
27. Cembrano, J. & Lara, L. The link between volcanism and tectonics in the southern volcanic zone of the Chilean Andes: a review. *Tectonophysics* **471**, 96–113 (2009).
28. Rowland, J. V. & Simmons, S. F. Hydrologic, magmatic, and tectonic controls on hydrothermal flow, Taupo volcanic zone, New Zealand: implications for the formation of epithermal vein deposits. *Econ. Geol.* **107**, 427–457 (2012).
29. Zajacz, Z., Seo, H., Candela, P. A., Piccoli, P. M. & Tossell, J. A. The solubility of copper in high-temperature magmatic vapors: a quest for the significance of various chloride and sulfide complexes. *Geochim. Cosmochim. Acta* **75**, 2811–2827 (2011).
30. Hogg, O. R., Edmonds, M. & Blundy, J. Water-rich magmas optimize volcanic chalcophile element outgassing fluxes. *Earth Planet. Sci. Lett.* **611**, 118153 (2023).
31. Chiaradia, M. Copper enrichment in arc magmas controlled by overriding plate. *Nat. Geosci.* **7**, 43–46 (2014).
32. Lee, C. –T. A. et al. Copper systematics in arc magmas and implications for crust-mantle differentiation. *Science* **336**, 64–68 (2012).
33. Zajacz, Z. & Halter, W. Copper transport by high temperature, sulfur-rich magmatic vapor: evidence from silicate melt and vapor inclusions in a basaltic andesite from the Villarrica volcano (Chile). *Earth Planet. Sci.* **282**, 115–121 (2009).
34. Sánchez-Alfaro, P. et al. Physical, chemical and mineralogical evolution of the Tolhuaca geothermal system, southern Andes, Chile: Insights into the interplay between hydrothermal alteration and brittle deformation. *J. Volcanol. Geotherm. Res.* **324**, 88–104 (2016).
35. Tardani, D. et al. Copper–arsenic decoupling in an active geothermal system: a link between pyrite and fluid composition. *Geochim. Cosmochim. Acta* **204**, 179–204 (2017).
36. Pérez-Flores, P. et al. Tectonics, magmatism and paleo-fluid distribution in a strike-slip setting: insights from the northern termination of the Liquiñe–Ofqui fault System, Chile. *Tectonophysics* **680**, 192–210 (2016).
37. Tardani, D. et al. Exploring the structural controls on helium, nitrogen and carbon isotope signatures in hydrothermal fluids along an intra-arc fault system. *Geochim. Cosmochim. Acta* **184**, 193–211 (2016).
38. Wrage, J. et al. Geochemistry of thermal waters in the Southern Volcanic Zone, Chile–implications for structural controls on geothermal fluid composition. *Chem. Geol.* **466**, 545–561 (2017).
39. Pérez-Estay, N. et al. Decoding the state of stress and fluid pathways along the Andean Southern Volcanic Zone. *Commun. Earth Environ.* **4**, 390 (2023).
40. Tassara, A. & Echaurren, A. Anatomy of the Andean subduction zone: three-dimensional density model upgraded and compared against global-scale models. *Geophys. J. Int.* **189**, 161–168 (2012).
41. Cembrano, J., Schermer, E., Lavenu, A. & Sanhueza, A. Contrasting nature of deformation along an intra-arc shear zone, the Liquiñe–Ofqui fault zone, southern Chilean Andes. *Tectonophysics* **319**, 129–149 (2000).
42. Pérez-Flores, P. et al. Fracture network, fluid pathways and paleostress at the Tolhuaca geothermal field. *J. Struct. Geol.* **96**, 131–148 (2017).
43. Tibaldi, A., Bonali, F. L., & Corazzato, C. Structural control on volcanoes and magma paths from local- to orogen-scale: the central Andes case. *Tectonophysics* **699**, 16–41 (2017).
44. Arnórsson, S., Stefánsson, A. & Bjarnason, J. O. Fluid-fluid interactions in geothermal systems. *Rev. Mineral. Geochem.* **65**, 259–312 (2007).
45. Symonds, R. B., Gerlach, T. M. & Reed, M. H. Magmatic gas scrubbing: implications for volcano monitoring. *J. Volcanol. Geotherm. Res.* **108**, 303–341 (2001).
46. Sano, Y., Marty, B. & Burnard, P. in *The Noble Gases as Geochemical Tracers. Advances in Isotope Geochemistry* (ed. Burnard, P.) 17–31 (Springer-Verlag, 2013).
47. Morrison, P. & Pine, J. Radiogenic origin of the helium isotopes in rock. *Ann. N. Y Acad. Sci.* **62**, 71–92 (1995).
48. Graham, D. W. Noble gas isotope geochemistry of mid-ocean ridge and ocean island basalts: characterization of mantle source reservoirs. *Rev. Mineral. Geochem.* **47**, 247–317 (2002).
49. Obase, T. et al. Monitoring of magmatic–hydrothermal system by noble gas and carbon isotopic compositions of fumarolic gases. *Sci. Rep.* **12**, 17967 (2022).
50. Hilton, D. R., Hammerschmidt, K., Teufel, S. & Friedrichsen, H. Helium isotope characteristics of Andean geothermal fluids and lavas. *Earth Planet. Sci. Lett.* **120**, 265–282 (1993).
51. Roulleau, E. et al. Multi-element isotopic evolution of magmatic rocks from Caviahue-Copahue Volcanic complex (Chile-Argentina): involvement of mature slab recycled materials. *Chem. Geol.* **476**, 370–388 (2018).
52. Lages, J. et al. Crustal controls on light noble gas isotope variability along the Andean Volcanic Arc. *Geochem. Perspect. Lett.* **19**, 45–49 (2021).
53. Edmonds, M., Mason, E. & Hogg, O. Volcanic outgassing of volatile trace metals. *Annu. Rev. Earth Planet. Sci.* **50**, 79–98 (2022).
54. Edmonds, M., Mather, T. & Liu, E. J. A distinct metal fingerprint in arc volcanic emissions. *Nat. Geosci.* **11**, 790–794 (2018).
55. Audétat, A. & Edmonds, M. Magmatic-hydrothermal fluids. Elements: an international magazine of mineralogy. *Geochem. Petrol.* **16**, 401–406 (2020).
56. Hartley, M. E., Maclennan, J., Edmonds, M. & Thordarson, T. Reconstructing the deep CO2 degassing behaviour of large basaltic. *Earth Planet. Sci. Lett.* **393**, 121–131 (2014).
57. Taran, Y. A., Hedenquist, J. W., Korzhinsky, M., Tkachenko, S. I. & Shmulovich, K. I. Geochemistry of magmatic gases from Kudryavy volcano, Iturup, Kuril Islands. *Geochim. Cosmochim. Acta* **59**, 1749–1761 (1995).
58. Reich, M. et al. Pyrite as a record of hydrothermal fluid evolution in a porphyry copper system: A SIMS/EMPA trace element study. *Geochim. Cosmochim. Acta* **104**, 42–62 (2013).
59. Tassara, S. et al. Highly siderophile elements mobility in the subcontinental lithospheric mantle beneath southern Patagonia. *Lithos* **314**, 579–596 (2018).
60. Heinrich, C. A. & Connolly, J. A. Physical transport of magmatic sulfides promotes copper enrichment in hydrothermal ore fluids. *Geology* **50**, 1101–1105 (2022).
61. Sillitoe, R. H. Iron oxide-copper-gold deposits: an Andean view. *Min. Depos.* **38**, 787–812 (2003).
62. Barton, M. D. Iron oxide(-Cu-Au-REE-P-Ag-U-Co) systems. In *Treatise on Geochemistry*. (eds. Holland, H. D. & Turekian, K. K.) (second edition) p. 515–541 (Elsevier, Oxford, UK, 2014).
63. Reich, M. et al. Formation of iron oxide–apatite deposits. *Nat. Rev. Earth Environ.* **3**, 758–775 (2022).

64. Barra, F. et al. Unraveling the origin of the Andean IOCG clan: a Re-Os isotope approach. *Ore Geol. Rev.* **81**, 62–78 (2017).
65. del Real, I. et al. Formation of giant iron oxide-copper-gold deposits by superimposed episodic hydrothermal pulses. *Sci. Rep.* **13**, 12041 (2023).
66. Roulleau, E. et al. New insight from noble gas and stable isotopes of geothermal/hydrothermal fluids at Caviahue-Copahue Volcanic Complex: boiling steam separation and water-rock interaction at shallow depth. *J. Volcanol. Geotherm. Res.* **328**, 70–83 (2016).
67. Craig, H., Lupton, J. E. & Horibe, Y. in *Terrestrial Rare Gases. Advances in Earth and Planetary Science* (eds. Alexander and M. Ozima) 3–16 (Academic Publication, 1978).

Acknowledgements

We gratefully acknowledge funding provided by the Chilean National Agency of Research and Development (FONDECYT *Iniciación* #11220777 to D.T., FONDECYT *Regular* #1201219 to P.S.-A., FONDECYT *Iniciación* #11190846 to P.R., FONDECYT Iniciación #11240035 to S.T.; ANID Anillo #ATE220029 to D.T., and FONDAP #ACE210005). Additional support was provided by NSERC Discovery Grant no. RGPIN-2020-04684 and FRQNT (Regroupement Stratégiques) no. 2024-RSMA-341269 to D.P., FONDECYT #1210591 to J.C. and P.P.-F., and the Millennium Science Initiative Program (grant NCN13_065) to M.R. We also thank Tom Grelet for assistance with the helium isotopic analyses. This work was financed by the Publications Support Fund of the Universidad de O'Higgins.

Author contributions

D.T., S.T., and M.R. designed the study and developed the project. D.T., P.R., and P.S.-A. did the fieldwork and collected the samples. D.T. and S.T. wrote the manuscript and made the figures. P.P.F. and J.C. performed the structural analysis. D.P. performed the He isotope analyses. C.C. and J.J.A. provided perspectives and conceptual advice on model development. All authors discussed interpretations of results and their implications.

Competing interests

The authors declare no competing interests.

Additional information

Supplementary information The online version contains supplementary material available at https://doi.org/10.1038/s43247-024-01629-8.

Correspondence and requests for materials should be addressed to Daniele Tardani or Santiago Tassara.

Peer review information *Communications Earth & Environment* thanks Tomoya Obase and the other, anonymous, reviewer(s) for their contribution to the peer review of this work. Primary handling editors: Derya Gürer and Carolina Ortiz Guerrero. A peer review file is available.